ACSNANO

www.acsnano.org

Dynamic Modeling of a Stream-Current-Based Microfluidic Nanogenerator

Jingwen Zhang, Jiajia Shao,* Hadrien Monluc, Di Wei, Jing You, Liyun Ma, Liming Ding, Zhong Lin Wang,* and Shuge Dai*

Cite This: *ACS Nano* 2025, 19, 41330−41341 **Read Online**

ABSTRACT: **A microfluidic nanogenerator (MF-NG) that utilizes stream current is developed to convert fluidic hydropower into a continuous direct current (DC) output, demonstrating superior performance and distinct advantages in ion transport manipulation and energy harvesting. Despite its promise, the operational mechanisms of this technology remain insufficiently understood. In this study, we establish a theoretical model for the MF-NG, simulating and analyzing the ion transport system within micro/nanoscale channels by coupling the Poisson equation, Nernst−Planck equation, and Navier−Stokes equation. We present a comprehensive theoretical framework that elucidates the dynamic interaction and equilibrium between displacement current and ionic transport current. Our findings offer a detailed understanding of electrokinetic energy conversion in MF-NGs. Key factors such as pressure, solution concentration, and surface charge, along with the effects of barrier electric fields, play crucial roles in determining charge distribution polarization and facilitating the establishment of the induced streaming electric field, leading to the formation of streaming potential. This work outlines an interdependent chain of constraints governing electrokinetic phenomena in pressure-driven flows, providing a solid theoretical foundation for the design and optimization of streaming-potential-based MF-NGs.**

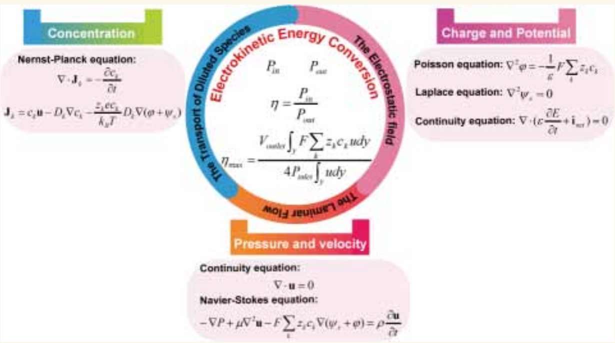

KEYWORDS: *microfluidic nanogenerator, electrical double layer, micro/nanofluidics, electrokinetic effect, displacement current*

1. INTRODUCTION

Streaming potential, one of the four principal electrokinetic phenomena in micro- and nanofluidics, has been widely reported for its applications in energy conversion as well as flow rate and concentration sensing.[1,2] Microfluidic nanogenerators (MF-NGs) leveraging streaming potential convert fluidic hydropower into continuous direct current (DC), representing a transformative platform for harvesting water-based energy.[3−5] Although MF-NGs encompass a variety of channel architectures, ranging from simple micro/nanochannels without internal structures to those with porous morphologies,[6−8] their underlying working mechanism remains fundamentally consistent. The channel walls acquire charge through liquid−solid contact electrification, resulting in the formation of a charged, thin liquid layer near the surface that neutralizes the solid wall charge.[9−11] This interfacial region is known as the electrical double layer (EDL). Upon application of pressure, mobile EDL segments enable selective ion enrichment and depletion at channel inlets and outlets, establishing a potential difference across the channel.[4,12,13] This potential difference, in turn, drives a unidirectional and continuous flow of electrons through an external circuit, generating a DC conduction current. The unique features of nanochannels, particularly the mobility of internal EDLs, render them an ideal platform for enabling this advanced mode of energy conversion. Despite their promise, existing literature presents relatively few theoretical investigations into the fundamental mechanisms underlying this process.[3,4,14−16]

Significant efforts have been made to enhance MF-NG performance by optimizing working fluids, channel materials, and channel geometries. However, a comprehensive understanding of the governing mechanisms and the quantitative relationships dictating energy conversion efficiency is still lacking. This gap primarily arises due to the absence of robust theoretical models capable of accurately linking the relevant physical parameters in the streaming potential phenomenon.

Received: September 15, 2025
Revised: November 24, 2025
Accepted: November 25, 2025
Published: November 30, 2025

ACS Publications

https://doi.org/10.1021/acsnano.5c15914

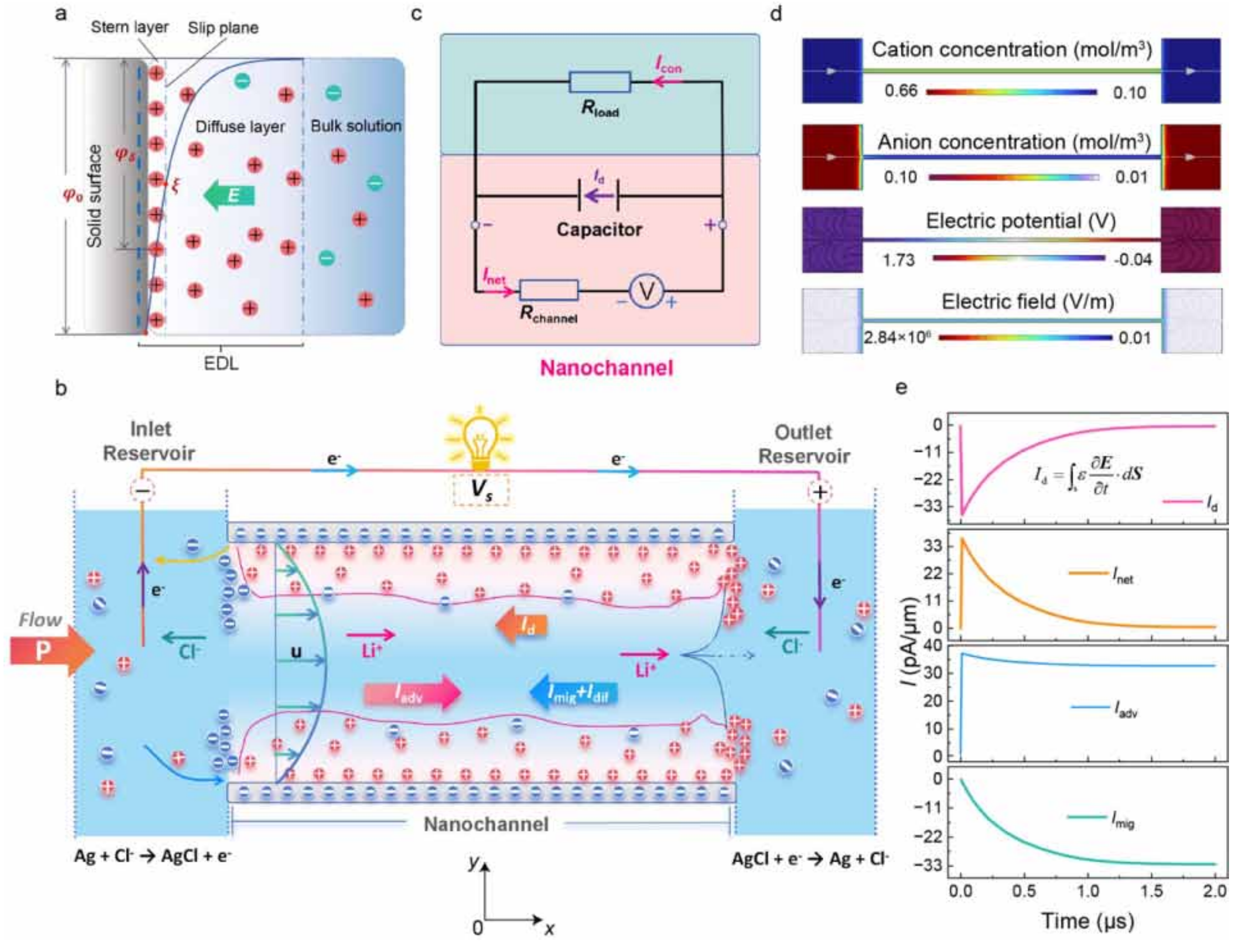

Figure 1. Theoretical modeling of a microfluidic nanogenerator (MF-NG) based on electric double layers (EDLs) and electro-kinetic effect. (a) Classic models of traditional EDLs. (b) Schematic diagram of the MF-NG. (c) Equivalent circuit model of the MF-NG. (d) The distributions of the counterions concentration, co-ions concentration, potential, and electric field in the microchannel domain under steady state. (e) The corresponding displacement, net current, advection current, and migration current flowing at the midlength of the channel, respectively.

For example, while the Maxwell displacement current is recognized as the primary driving force in traditional triboelectric nanogenerators (TENGs),[17,18] it remains unclear whether an analogous displacement current governs the core operation of MF-NGs—even though a time-varying electric field is known to arise during their operation.

In this work, we construct a multidisciplinary theoretical model to emulate the fundamental processes of MF-NGs and elucidate the origins, dynamic evolution, and physical consequences of both ionic concentration polarization and charge spatial distribution polarization. Through parametric analysis, we uncover how key physical quantities dynamically respond to external forces and material properties, revealing the mechanisms by which various parameters influence ionic selectivity and permeability. We further derive analytical expressions for maximum output power and energy conversion efficiency. Systematic mapping of system response elucidates the interplay between applied pressure, bulk electrolyte concentration, electrolyte type, and channel surface charge density on key electrical output characteristics. Most importantly, we identify, a persistent dynamic equilibrium between displacement current and net ionic transport current. The theoretical framework and analysis developed here are anticipated to advance the mechanistic understanding of MF-NGs and inform further device optimization.

2. RESULTS AND DISCUSSION

2.1. Electrical Double Layers. The electrical double layer (EDL) refers to the arrangement of electric charges at the interface between a solid surface and an adjacent liquid. Upon contact with an electrolyte solution, the solid surface acquires a charge via mechanisms such as ionization, ion adsorption, or redox reactions. To maintain electroneutrality, counterions in the solution accumulate near the charged surface while co-ions are repelled, resulting in the formation of a double layer. The EDL plays a critical role in electrokinetic phenomena, capacitive energy storage, and electrophoresis. Recent studies have clarified that EDL formation involves at least a two-step process: first, electron transfer at the pristine surface, followed by the attraction of free ions from the solution to the charged surface, collectively establishing the EDL structure (Figure 1a).[19,20] Counterions adjacent to the wall form the immobile "Stern layer" due to strong electrostatic adsorption,[21] whereas ions beyond this region constitute the "diffuse layer," where their concentration gradually approaches the bulk value under the influence of thermal diffusion. The boundary separating these two regions is defined as the "slip plane," and the

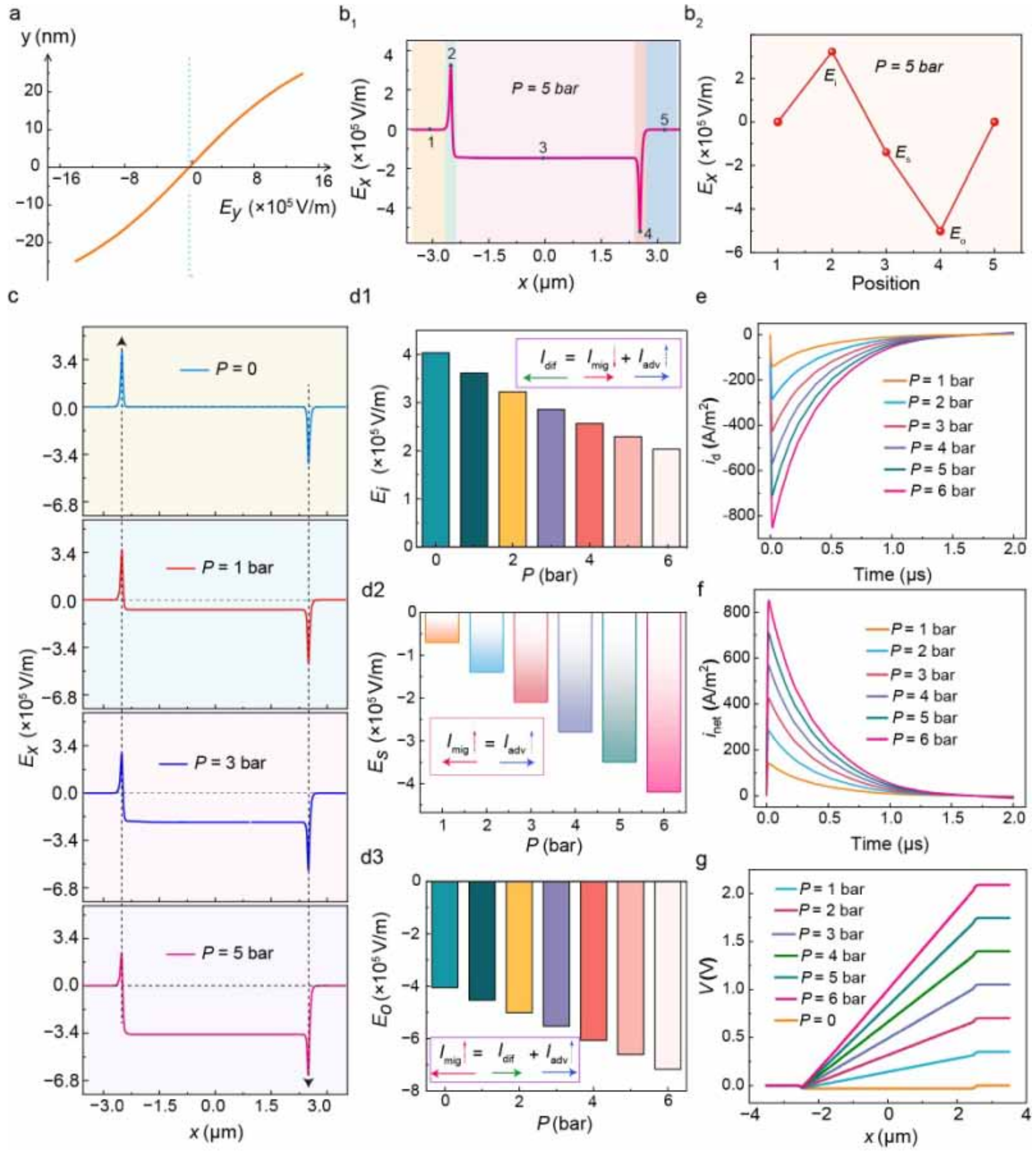

Figure 2. Effect of pressure on the output performance of the MF-NG. (a) EDL electric field along the *y*-axis under different pressure conditions. (b_1) Distribution of the streaming-induced electric field along the channel centerline, and (b_2) corresponding electric field strength distributed at the inlet pool, channel inlet, channel center, channel outlet, and outlet pool under a pressure *P* = 5 bar, respectively. (c) Distribution of the streaming-induced electric field along the channel centerline at steady state when *P* increases from 0 to 6 bar; and peak values of the streaming-induced electric field distributed at (d_1) the channel inlet, (d_2) the midpoint, (d_3) the channel outlet, respectively. (e) Transient net ionic current density, (f) transient displacement current density, and (g) the streaming potential from the inlet pool to the outlet pool along the centerline when *P* increases from 0 to 6 bar. The bulk concentration of LiCl aqueous solution and surface charge density are assumed to be 0.1 mM and −1 mC/m,² respectively.

potential at this location, assuming a zero potential far from the wall, is known as the "zeta potential".[22] The EDL thickness is characterized by the Debye length, given by[23]

$$\lambda_d = \left(\frac{\varepsilon k_B T}{\sum_{k=1}^{N} c_0 N_A z_k^2 e^2}\right)^{1/2} \tag{1}$$

where ε is the permittivity of the solution, k_B is the Boltzmann constant, T is the temperature, e is the elementary charge, c_0 is the bulk solution concentration, N_A is the Avogadro's constant, and z_k is the valence of the ion of species k. In dilute electrolyte solutions with concentrations ranging from 10^{-6} to 10^{-2} m, the thickness of the electric double layer varies from several nanometers to several hundred nanometers.[24] Outside the EDL, the solution maintains electrical neutrality.

2.2. Geometry and Mechanism of the MF-NG. In this work, we design a microfluidic channel with a height comparable to the thickness of the EDL and a length on the micron scale. The nanochannel connects two reservoirs filled with a dilute electrolyte (e.g., LiCl), facilitating fluid flow between them. Applying pressure from the inlet reservoir drives liquid toward the outlet (Figure 1b). For simulation, a representative rectangular cross-section along the flow direction is selected, defining the channel centerline as the *x*-axis (origin at the midpoint), and the *y*-axis perpendicular to the centerline. Upon liquid−solid contact electrification, the channel walls acquire negative charges, giving rise to EDLs near the walls; design parameters are provided in Table S1.

Since the channel height is on the order of the Debye length, significant concentration gradients arise for counterions and co-ions within the channel, particularly at the nanoscopic inlet and outlet (Figure S1).

When pressure is applied, excess counterions are advected by the fluid toward the outlet, forming the advective current I_{adv} (Figure 1c). The disparity in ion concentration between the channel and reservoirs induces an imbalance in flux at each interface, commonly termed streaming-driven space-charge separation. This manifests as counterion accumulation and co-ion depletion at the channel outlet, and the opposite at the inlet, resulting in the development of a streaming-induced electric field $\boldsymbol{E}_s$, which drives ions upstream, giving rise to a backflow migration current I_{mig}. As charge distribution polarization intensifies, $\boldsymbol{E}_s$ increases, and a displacement current I_d is generated. The net ion transport current I_{net} gradually diminishes as I_{mig} rises (Figure 1e), with I_d and I_{net} net always equal in magnitude but opposite in direction. I_d rises sharply at the onset, peaks, and then decays, capturing the time rate-of-change of $\boldsymbol{E}_s$, and serves as an indicator of both mass transfer and charge redistribution. At steady-state, the potential, electric field, and concentration distributions (Figure 1d) define a streaming potential (e.g., 1.73 V). To maintain electroneutrality, electrode reactions balance the system, ensuring persistent conduction current I_{con}, in the external circuit and net ion transport within the channel (Figure 1b).

2.3. Electrical Analogy. Figure 1c illustrates an equivalent circuit of the nanochannel, modeled as a voltage source in series with the channel resistance, R_{ch} and in parallel with capacitance C; the circuit includes a load resistance R_{load}, in series, dictating the voltage and current relationship. The conduction current I_{con} through the load equals I_{net} in the channel. Initially, prior to potential buildup, the only current in the channel is I_{adv}, arising from the transport of non-neutral electrolyte solution, corresponding to the short-circuit current I_{sc}, as the external voltage is zero and I_{con} equals I_{adv}.

As ion transport continues, charge distribution polarization expands across the channel, and a potential builds up between its ends. The capacitor reflects the potential difference, modulated by co-ion enrichment at the inlet and counterion enrichment at the outlet. The backflow migration current I_{mig} rises against the direction of flow, causing I_{net} to decline along the flow direction. Accordingly, I_{con} through R_{load} also decreases, while the terminal voltage increases in step with the nanochannel's potential difference and the charging of the capacitor. The displacement current I_d between capacitor plates and the external conduction current I_{con} are complementary in time and successive in space. This progression increases the ratio R_{load}/R_{ch}, thus raising the load voltage and reducing the current. When I_{mig} equals I_{adv}, I_{net} becomes zero, marking the steady-state potential difference V_s across across the nanochannel, the open-circuit voltage V_{oc} of the MF-NG. At this point, I_{con} vanishes and the maximum load voltage is attained. A rigorous proof of the equivalent circuit and corresponding equations are provided in Supplementary Notes 1 and 2, respectively.

2.4. Pressure Effect. The displacement current (I_d) serves not only as an indicator of the temporal evolution of the streaming-induced electric field but also provides insight into the progress of net charge transfer within the system. Pressure modulates ion selectivity by influencing the barrier electric fields at the channel interfaces ($\boldsymbol{E}_i$ and $\boldsymbol{E}_o$). Variations in the net ion transport current (I_{net}) give rise to streaming-driven space-charge separation, ultimately dictating the establishment and dynamics of the streaming-induced electric field ($\boldsymbol{E}_s$). The temporal evolution of $\boldsymbol{E}_s$ generates I_d, which continuously interacts with and balances I_{net}. The effects of pressure can be summarized as follows: (i) as the input pressure increases, both $\boldsymbol{E}_s$ and its rate of change with time increase; (ii) $\boldsymbol{E}_i$ decreases along the flow direction, while $\boldsymbol{E}_o$ increases in the reverse (outlet) direction; (iii) ion selectivity at the channel exit is enhanced, whereas selectivity at the entrance tends to decrease. An appropriately increased pressure thus strengthens the overall electrokinetic effect.

Applied pressure acts as the primary driving force for ion transport, directly determining the flow velocity in the nanochannel, and consequently controlling the magnitude of the advective current (I_{adv}). Within the investigated pressure range (0.1−0.6 MPa; see Table S1 for simulation parameters), Figure 2a illustrates the longitudinal electric field E_y where oppositely directed EDL electric fields are formed near the upper and lower walls, each pointing toward its respective "source", the surface negative charges. Due to equivalent surface charge densities, the two EDL electric fields are symmetrically distributed about the channel centerline. As the distance from the wall increases, the field decreases more gradually, attributed to lower net charge densities further from the interface. It is important to note that pressure does not affect EDL formation or E_y. The distribution of the transverse electric field (E_x) is depicted in Figure 2b1,b2, highlighting five regions from left to right: a zero field in the inlet reservoir; a spike (barrier) electric field ($\boldsymbol{E}_i$) pointing right at the nanochannel inlet; a uniform streaming-induced electric field ($\boldsymbol{E}_s$) pointing left within the channel; a spike electric field ($\boldsymbol{E}_o$) pointing left at the outlet; and a zero field in the outlet reservoir. Since both reservoirs are electrically neutral, the fields within them are zero. This study focuses on the regions near the channel interfaces as well as the streaming-induced field inside the nanochannel.

Figure 2c,d1−d3 illustrates the evolution of these fields as pressure increases from 0 to 6 bar. In the absence of applied pressure, only static EDLs exist, with no ion transport. The only nonzero transverse field is the spike at the channel entrances ($\boldsymbol{E}_i$), where steep and equal concentration gradients at both termini (Figure S1b) drive diffusion currents (opposite directions at entrance and exit). To maintain current continuity, the magnitudes of $\boldsymbol{E}_i$ and $\boldsymbol{E}_o$ must be equal (400 kV/m), directed right and left, respectively, to generate migration currents that counterbalance the respective diffusion contributions (Figure 2d1,d3). At the inlet, $\boldsymbol{E}_i$ "intercepts" nontarget ions (co-ions, Cl^-), facilitating target ion (counterion, Li^+) entry into the nanochannel. At the outlet, $\boldsymbol{E}_o$ "traps" target ions (Li^+) and removes residual co-ions from the channel, collectively establishing the system's ion selectivity.

With the gradual application and increase of pressure (0 to 6 bar), I_{adv} is generated and increases (Figure S2), while diffusive current (I_{dif}) at the channel interfaces remains essentially unchanged. To preserve current continuity, $\boldsymbol{E}_i$ at the channel inlet decreases, reducing I_{mig} and increasing I_{adv} to counteract the leftward I_{dif} (Figure 2d1). At the outlet, $\boldsymbol{E}_o$ intensifies in the leftward direction to balance both I_{dif} and the growing I_{adv} (Figure 2d3). Thus, ion permeability in the channel and ion selectivity at the outlet are enhanced, while selectivity at the inlet diminishes. In a highly selective channel, ion transport prompts streaming-driven space-charge separation (Figures S3 and S4). Counterions (Li^+) accumulate at the outlet, while co-

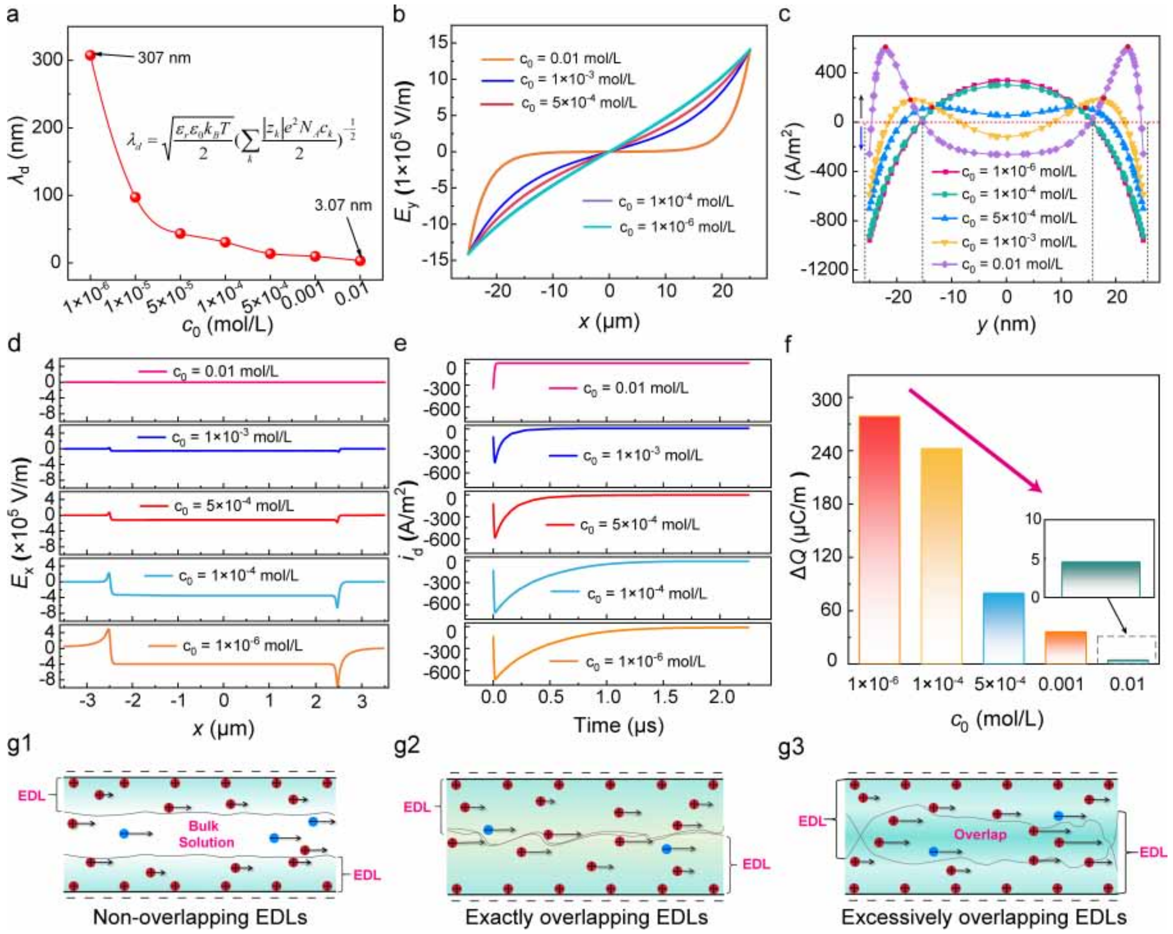

Figure 3. Effect of solution concentration on the output performance of the MF-NG. (a) Under initial concentration c_0 varying from 0.001 mM to 0.01 M, with a 0.5 MPa pressure-driven, and a fixed −1 mC/m^2 channel surface charge density, Debye length. (b) EDL electric field at the midlength. (c) Steady-state ionic net current along the *y*-axis. (d) Steady-state streaming-induced electric field along the channel centerline. (e) Transient displacement current density in the channel. (f) Transferred net charge quantity. (g1) Inside the channel of MF-NG, schematic diagrams of physical interpretations for the nonoverlapping EDLs. (g2) Inside the channel of MF-NG, schematic diagrams of physical interpretations for the exactly overlapping EDLs. (g3) Inside the channel of MF-NG, schematic diagrams of physical interpretations for the excessively overlapping EDLs.

ions (Cl$^-$) are depleted at the outlet but concentrated at the inlet as pressure increases. The resulting charge distribution polarization is shown in Figure S5, where net charges accumulate at the outlet and deplete at the inlet, generating a reverse streaming-induced electric field, a phenomenon readily explained by current balance. At larger pressures, I_{adv} becomes substantial while I_{dif} diminishes (Figure S6), reflecting the absence of a significant concentration gradient within the channel. Nonetheless, the generated reverse field gives rise to an increased I_{mig}, ensuring current continuity (Figure 2d2).

The displacement current (I_d) arises in the channel from variations in $\boldsymbol{E}_s$. As shown in Figure 2e, I_d is directly proportional to applied pressure, increasing rapidly to a peak within 0.01 μs, then gradually declining to zero. This trend indicates that $\boldsymbol{E}_s$ also climbs rapidly at first, then stabilizes within 2 μs, a behavior dictated by changes in net ion transport and charge distribution polarization. As pressure increases, I_{adv} rises accordingly, reinforcing the charge distribution polarization and promoting the growth of $\boldsymbol{E}_s$. Subsequently, I_{mig} increases to suppress the polarization, eventually resulting in a slow down of $\boldsymbol{E}_s$ variation. Conversely, I_{net} initially increases but then decreases with rising pressure (Figure 2f). As previously discussed, I_{net} represents the net charge transfer per unit time increasing (the sum of I_{adv}, I_{mig}, and I_{dif}); its time integral quantifies the total transferred charge. Increased pressure generates a larger I_{adv}, further polarizing charges and producing a substantial I_{mig} to offset the increased I_{adv} in the nanochannel. Steady state is achieved when I_{mig} and I_{adv} are equal, at which point I_{net} gradually decreases to zero. Notably, no conduction current is present in the external circuit at this stage. Corresponding potential (V) distributions along the channel centerline are depicted in Figure 2g, demonstrating that the streaming potential in both reservoirs is zero, while V within the nanochannel scales with applied pressure. (The spatial and temporal evolution of electric potentials and net transferred charge are provided in Figures S7 and S8, respectively.)

2.5. Concentration Effect. The concentration of the electrolyte solution is a crucial determinant of the output performance of MF-NGs. Parameters such as the Debye length (λ_d), EDL thickness, ion selectivity, and the streaming-induced electric field are all strongly dependent on the bulk solution concentration. The Debye length, which defines the characteristic scale of electrostatic screening by mobile charge carriers,[23,24] effectively delineates the thickness of the EDL.

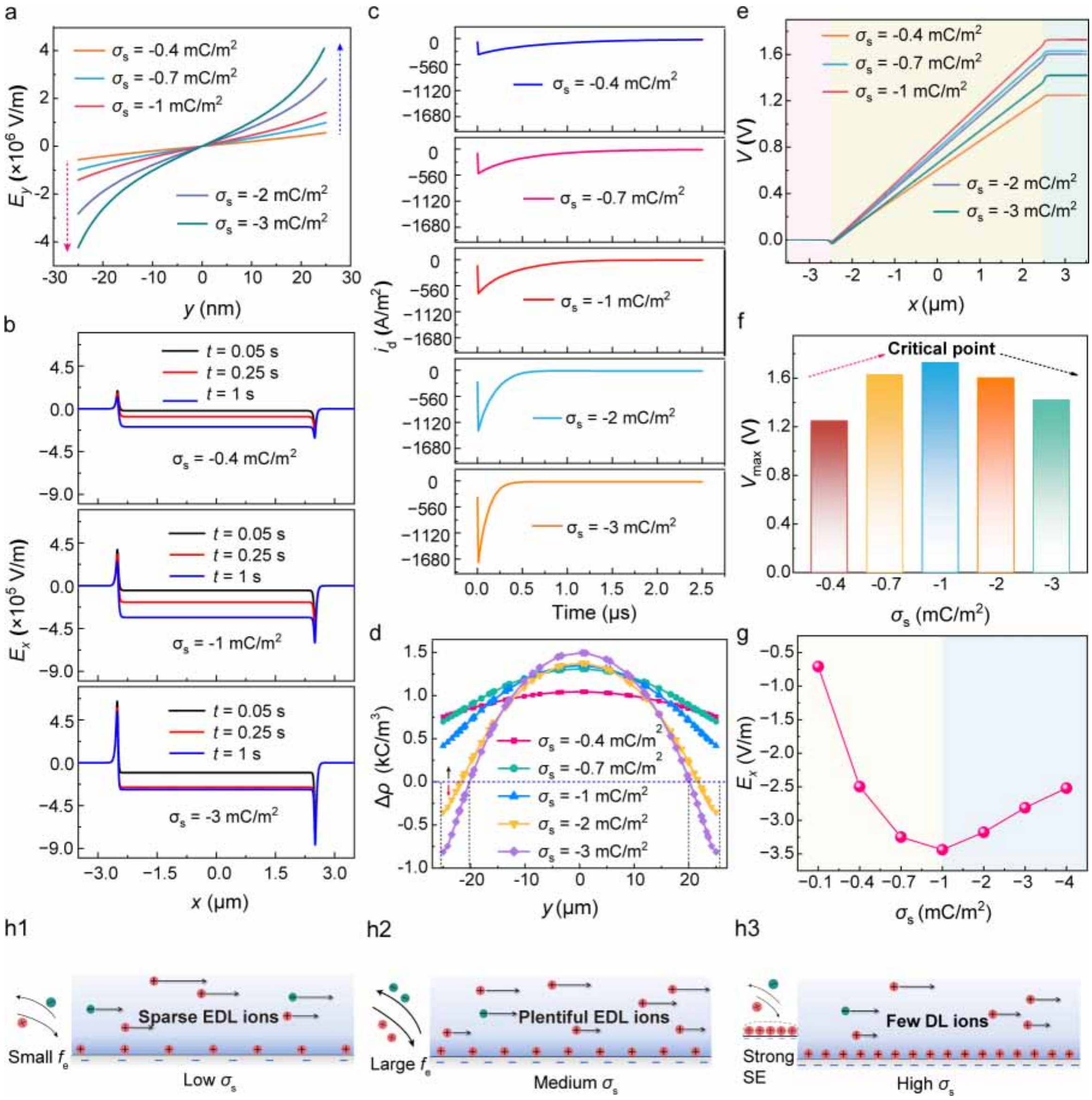

Figure 4. Effect of surface charge density on the output performance of the MF-NG. (a) EDL electric field along the *y*-axis with surface charge density σ_s varying from −0.4 mC/m^2 to −3 mC/m^2. (b) Distribution of the streaming-induced electric field along the channel centerline at *t* = 0.05 s, *t* = 0.25 s, and *t* = 1 s under various σ_s, respectively. For σ_s from −0.4 mC/m^2 to −3 mC/m,^{2} (c) transient displacement current density in the channel, (d) charge density variation before and after the transport process at various locations of the channel outlet, (e) distribution of the streaming potential from the inlet pool to the outlet pool along the centerline, (f) maximum potential in outlet pool, and (g) streaming-induced electric field at the channel center under steady state. Schematic diagrams of physical interpretations for (h_1) low surface charge density, (h_2) medium surface charge density, and (h_3) high charge density.

Generally, a larger λ_d corresponds to a thicker EDL. As shown in Figure 3a, λ_d is inversely proportional to the solution concentration (c_0); for example, λ_d reaches 307 nm at $c_0 = 1 \times 10^{-6}$ mol/L, and declines to 3.07 nm at c_0 = 0.01 mol/L (Figure 3a). Thus, increasing the bulk concentration results in a thinner EDL. Within the channel, pairs of oppositely directed electric fields develop near the upper and lower walls, oriented toward the respective surface charges. Simulations were performed over a concentration range of 0.001 to 10 mM; the complete parameter sets are provided in Table S1.

The total longitudinal electric field (E_y) consists of the y-components of the local electric fields within the EDL. The distribution of E_y changes distinctly with c_0 (Figure 3b), maintaining symmetry across the channel centerline and consistently vanishing at the origin. When c_0 = 0.01 mol/L, the corresponding λ_d (3.07 nm) is much smaller than the channel height (H = 50 nm). In the spatial range y = −10 to 10 nm, the strength of E_y falls to zero, reflecting the presence of an electrically neutral bulk solution region (Figure 3b). This result indicates that EDLs occupy a minimal fraction of the channel at higher concentrations (Figure 3g1). As c_0 decreases, the effective spatial utilization of the EDL increases (Figure 3g2), reaching full overlap at strongly dilute concentrations (e.g., $c_0 = 1 \times 10^{-6}$ mol/L), where EDLs originating from opposite walls interact and overlap, producing a net field of zero at the channel center (Figure 3g3). In addition, the decay length of E_y away from the wall increases with dilution (Figure 3b).

Distributions of the I_{net}, I_{adv}, and I_{mig} along the *y*-axis are presented in Figure 3c, and Figure S9, respectively. At low concentrations ($c_0 = 1 \times 10^{-6}$ mol/L, and 1×10^{-4} mol/L),

I_{net} is positive near the channel centerline (approximately 15.3 nm from the wall) but negative within about 5 nm of the wall. Increasing c_0 above 1×10^{-3} mol/L causes I_{net} near the centerline to become negative, with two positive peaks near the walls. These current distributions are the result of competing influences from I_{adv}, I_{dif}, and I_{mig}. Under strongly dilute conditions, EDLs from both channel walls overlap, rendering the channel center nonelectroneutral and reducing central flow velocity (Figure S10a−d). Consequently, the profile of I_{adv} adopts an arched shape (Figure S9a). Although I_{mig} also exhibits a similar structure (Figure S9b), the high net charge density sustains a nearly constant total current (I_{net}) along the y-axis. As c_0 increases (e.g., to 5×10^{-4} mol/L), the EDLs begin to separate, increasing central flow velocity but reducing net charge density, leading to a lowered I_{adv} at the centerline (Figure S9a). The corresponding I_{mig}, which opposes I_{adv}, is more evenly distributed (Figure S9b), and the net current in the central region decreases but remains positive. At even higher concentrations, the nonoverlapping, thin EDL restricts significant net charge to the channel edge, maximizing central flow velocity and minimizing I_{adv}, so the total net current is reduced and eventually reverses direction with further increase in c_0 (Figure 3c).

The dependence of the x-component of the electric field ($\boldsymbol{E}_x$) on c_0 is illustrated in Figure 3d. As c_0 decreases, the inlet electric field ($\boldsymbol{E}_i$) increases toward the right, while the outlet field ($\boldsymbol{E}_o$) grows in the opposite direction, exhibiting mirror symmetry. The streaming-induced electric field ($\boldsymbol{E}_s$) remains uniform within the channel but increases against the flow direction with decreasing c_0. These effects result from ion concentration polarization (Figure S11): more dilute solutions yield thicker EDLs and greater EDL utilization within the channel, which diminishes ionic liquid velocity along the channel centerline and increases accumulation of counterions (Li^+) and co-ions (Cl^-) at the outlet and inlet, respectively, thereby enhancing $\boldsymbol{E}_s$. Simultaneously, higher negative charge density at the channel inlet causes a pronounced increase of $\boldsymbol{E}_i$ at lower c_0 (Figure 3d), and a corresponding increase in $\boldsymbol{E}_o$ is observed at the channel outlet. The temporal variation in $\boldsymbol{E}_s$ generates the associated displacement current (I_d), which is distributed across the nanochannel section (Figure 3e). The peak value of I_d decreases with increasing c_0, although the peak always occurs at 0.01 μs. There is no doubt that the number of charge carriers decrease with decreasing c_0, thus generating a pronounced increase of $\boldsymbol{E}_i$ (Figure 3d) and a corresponding increase of displacement current. Notably, the time required for I_d to decline to zero increases as c_0 decreases. This reflects differences in ion flux between dilute and concentrated solutions, a lower c_0 produces reduced ion flux and thus requires more time for charge distribution polarization to reach steady state. Consistently, the total net charge transported decreases as c_0 increases (Figure 3f), since a higher concentration produces a thinner EDL. In this limit, a wider neutral solution region exists near the channel centerline, contributing negligibly to ion transport due to a lack of net charge. Therefore, dilute solutions, by promoting thicker EDLs, facilitate more effective net charge transport within the nanochannel.

2.6. Charged Surface. Contact electrification between the ionic liquid and the nanochannel wall results in the generation and distribution of triboelectric charges on the channel surface. The surface charge density (σ_s) of the wall is a critical parameter that profoundly influences electric field distribution, displacement current, net charge density (Figures S12 and S13), streaming potential, and the overall output performance of the MF-NG. Notably, variations in σ_s can modulate the electric fields at both the channel inlet and outlet, thereby shaping ion selectivity. Across the investigated range of σ_s (−0.1 to −3 mC/m^2; see Table S1 for additional simulation parameters), Figure 4a presents the distribution of E_y for different σ_s values. Here, E_y is approximately proportional to σ_s, reaching a maximum at the solid−liquid interface and diminishing to zero at the channel centerline, while maintaining symmetry about the center. This behavior derives from the spatial arrangement of counterions within the EDL: higher σ_s induces greater counterion accumulation near the wall, creating an enhanced shielding effect. As a result, ion concentration and electrostatic attraction in the channel center are both substantially reduced.

Additionally, as σ_s increases, the peaks of E_x at both channel entrance and exit grow larger; meanwhile, the peak of E_y at the entrance decreases, while the peak at the exit increases over time (Figure 4b). Importantly, E_x within the channel is uniformly distributed in proportion to σ_s. This arises mainly due to the increased concentration gradient at the channel interfaces (Figure S12b−d), which leads to greater accumulation of co-ions and counterions at the channel entrance and exit, respectively. Accumulation of charge at the interfaces enhances the magnitude of E_x in the bulk channel. It is also notable that while an increase in fixed wall charge density (σ_s) suppresses flow velocity (Figure S13), it simultaneously increases the net charge within the channel, enhancing both I_{adv} and $\boldsymbol{E}_s$. For example, the maximum $\boldsymbol{E}_s$ is achieved at σ_s = −1 mC/m^2, t = 1 s. However, excessively large σ_s values (e.g., −3 mC/m^2) attract a high concentration of counterions to the wall, which impedes solution flow and leads to minimal contribution to net current density in stagnant regions, thereby suppressing further formation of concentration polarization. This phenomenon explains why the highest streaming potential at steady state is observed at σ_s = −1 mC/m^2 (Figure 4e,f). The dependence of the streaming current on σ_s is further detailed in Figure S14.

As discussed previously, the time variation of $\boldsymbol{E}_s$ induces a displacement current (I_d) (Figure 4c). I_d rapidly reaches its peak, which scales proportionally with σ_s. This swift rise is attributed to an abrupt change in $\boldsymbol{E}_s$ driven by the rapid initial increase of I_{adv} within the first 0.01 μs (Figure 4b). Incremental increases in σ_s boost the net charge within the channel, accelerating the development of the streaming potential and the growth rate of $\boldsymbol{E}_s$. However, elevated net charges also reduce the time required for space-charge separation to reach saturation, leading to a shorter duration for I_d to stabilize at higher σ_s. Thus, increasing σ_s does not always result in a proportional enhancement (Figure 4g). To elucidate the complex relationship between net charge density ρ_e and σ_s, the distribution of ρ_e is quantitatively evaluated in Figure 4d. Notably, counterion accumulation near the channel centerline becomes increasingly prominent at higher σ_s, contrasting with the ion distribution observed outside the channel (Figure 4h1−h3). It should be noticed that the above model of the MF-NG is established at a neutral pH system, as it directly represents a highly relevant condition. Our primary goal is to present a comprehensive theoretical framework to explore the dynamic interaction and equilibrium between displacement current and ionic transport current. So, the important factors such as applied pressure, solution concentration, and surface charge are investigated systematically. It cannot be denied that pH is also an important parameter that controls surface charge of the channel wall. Exploring the full parameter space of pH, which would involve a systematic variation of surface charge, is an extensive endeavor that we believe warrants a separate, detailed investigation in our next work.

2.7. Basic Output Performance. We now turn to the fundamental output performance of the MF-NG device, highlighting the interrelationships among its physical quantities, the maximization of output power, and energy conversion efficiency. The output conduction current of the MF-NG is generally equivalent to the net ionic current resulting from internal mass transport processes.[25] The advective current I_{adv} and V_s correspond, respectively, to the short-circuit current (I_{sc}) and the open-circuit voltage (V_{oc}). Maximum output power is achieved when the external circuit resistance equals the device's internal resistance. In this study, we examined three symmetric electrolytes, LiCl, NaCl, and KCl, to evaluate the output performance characteristics of the MF-NG. The effects of applied pressure (P) on output parameters are shown in Figure 5a−c. As previously discussed, increasing the pressure results in higher V_s and I_{adv}, which in turn enhance both V_{oc} and maximum output power (P_{max}). However, the energy conversion efficiency (η_{max}) exhibits a gradual decline even as the mechanical input power increases. This trend is readily explained: indiscriminately increasing pressure can undermine ion selectivity. Furthermore, V_{oc}, P_{max} and η_{max} display a nonmonotonic dependence on electrolyte concentration (c_0; see Figure 5d−f), a phenomenon primarily governed by the interplay between EDL structure and bulk conductivity as c_0 varies (Figure S15). At low c_0, overlapping EDLs slightly raise the mobile charge density. As c_0 increases and EDL thickness decreases, charge confinement intensifies at channel interfaces, and the channel approaches a quasi-electroneutral state. Here, theoretical results in Figure 5d−f are obtained according to the eqs S16, S21, and S23 in the Supplementary Note 2, respectively. Adding fitting lines for these Figures would strengthen the analytical depth and provide better mechanistic insights. The variation of short-circuit current with pressure and c_0 is presented in Figure S16, while Figures S17−S19 describe the impact of geometric scaling on MF-NG output performance.

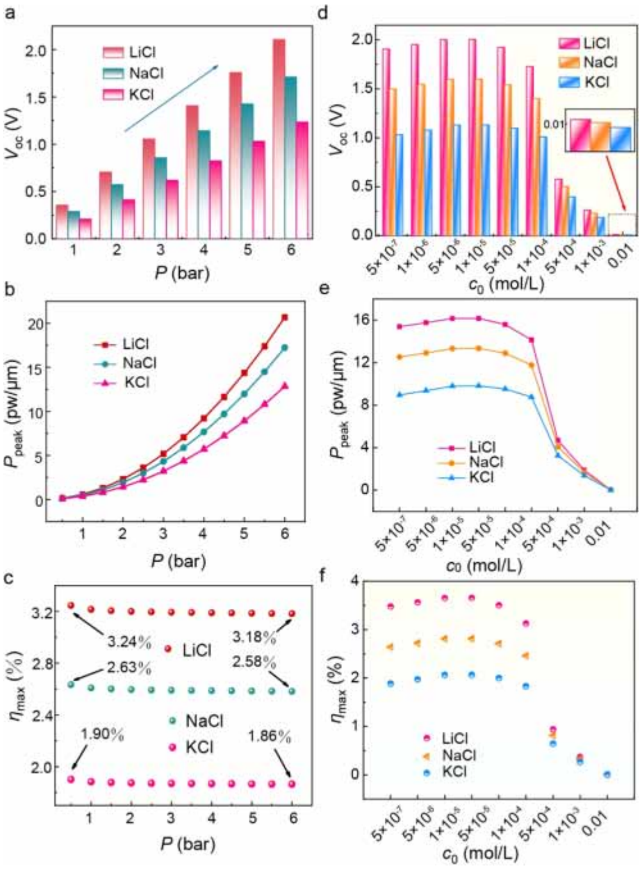

Figure 5. Basic output performance of the MF-NG under different pressure, solution concentration, and surface charge density, respectively. (a) Open-circuit voltage, (b) maximum output power, and (c) maximum output efficiency under various pressure conditions when c_0 = 0.1 mM, σ_s = −1 mC/m^2. (d) Open-circuit voltage, (e) maximum output power, and (f) maximum output efficiency under various solution concentration conditions when P = 5 bar, σ_s = −1 mC/m^2.

2.8. Ion Species. The ionic species, encompassing both valence and diffusion characteristics-exert a significant influence on the MF-NG's output behavior. To systematically assess these effects, we examined several electrolyte systems: monovalent symmetric solutions (LiCl, NaCl, KCl), divalent symmetric solutions ($MgSO_4$, $CuSO_4$, $CaSO_4$), and multivalent asymmetric solutions (Li_2SO_4, Na_2SO_4, K_2SO_4). The corresponding numerical results are shown in Figure 6a−f. Notably, the output parameters follow the order $Li^+ > Na^+ > K^+$ and $Mg^{2+} > Cu^{2+} > Ca^{2+}$, indicating that divalent asymmetric electrolytes yield higher V_{oc} and P_{max}. This behavior stems from two principal factors: ionic valence and diffusion coefficients. Cations such as Mg^{2+}, Cu^{2+}, and Ca^{2+} possess greater charges, producing thicker EDLs but also resulting in a reduced net charge flux (i.e., lower I_{adv}). Figure 6c displays the diffusion coefficients of the ions investigated: 1.03×10^{-9} (Li^+), 1.33×10^{-9} (Na^+), 1.96×10^{-9} (K^+), 2.03×10^{-9} (Cl^-), 1.07×10^{-9} (SO_4^{2-}), 0.705×10^{-9} (Mg^{2+}), 0.714×10^{-9} (Cu^{2+}), 0.792×10^{-9} (Ca^{2+}), and 0.541×10^{-9} m^2/s (Al^{3+}), respectively.[26,27] Divalent cations exhibit lower diffusion coefficients than monovalent cations, resulting in reduced bulk conductivity (κ), as governed by eq S6. Consistent with eq S15, the V_{oc} of divalent symmetric electrolytes is thus lower than that of monovalent symmetric counterparts, enabling construction of Figure 6g using eqs S16 and S21. These theoretical results and simulation conclusions are consistent with the previously published experimental data,[8,23,25,26] confirming the effectiveness and reliability of the built models.

Similarly, the output performance of monovalent symmetric electrolytes (LiCl, NaCl, KCl) surpasses that of multivalent symmetric electrolytes (Li_2SO_4, Na_2SO_4, K_2SO_4) (Figure 6d,e). Internal resistance (R_{ch}) is also a key parameter in MF-NG operation. For instance, although $MgSO_4$ cations are twice as highly charged as those in LiCl (Figure 6f), their diffusion coefficient is less than half that of LiCl (Figure 6e), resulting in an R_{ch} for $MgSO_4$ approximately half that for LiCl according to eqs S20 and S21. Therefore, optimal matching conditions yield the results presented in Figure 6g,h, consistent with eqs S15 and S16. Of note, if the nanochannel wall becomes positively charged, ion selectivity is reversed, as schematically illustrated by the ion transport systems in Figure 6i1,i2. The variation in bulk conductivity across different electrolyte systems is shown in Figures S20−S22. In summary,

https://doi.org/10.1021/acsnano.5c15914
ACS Nano 2025, 19, 41330−41341

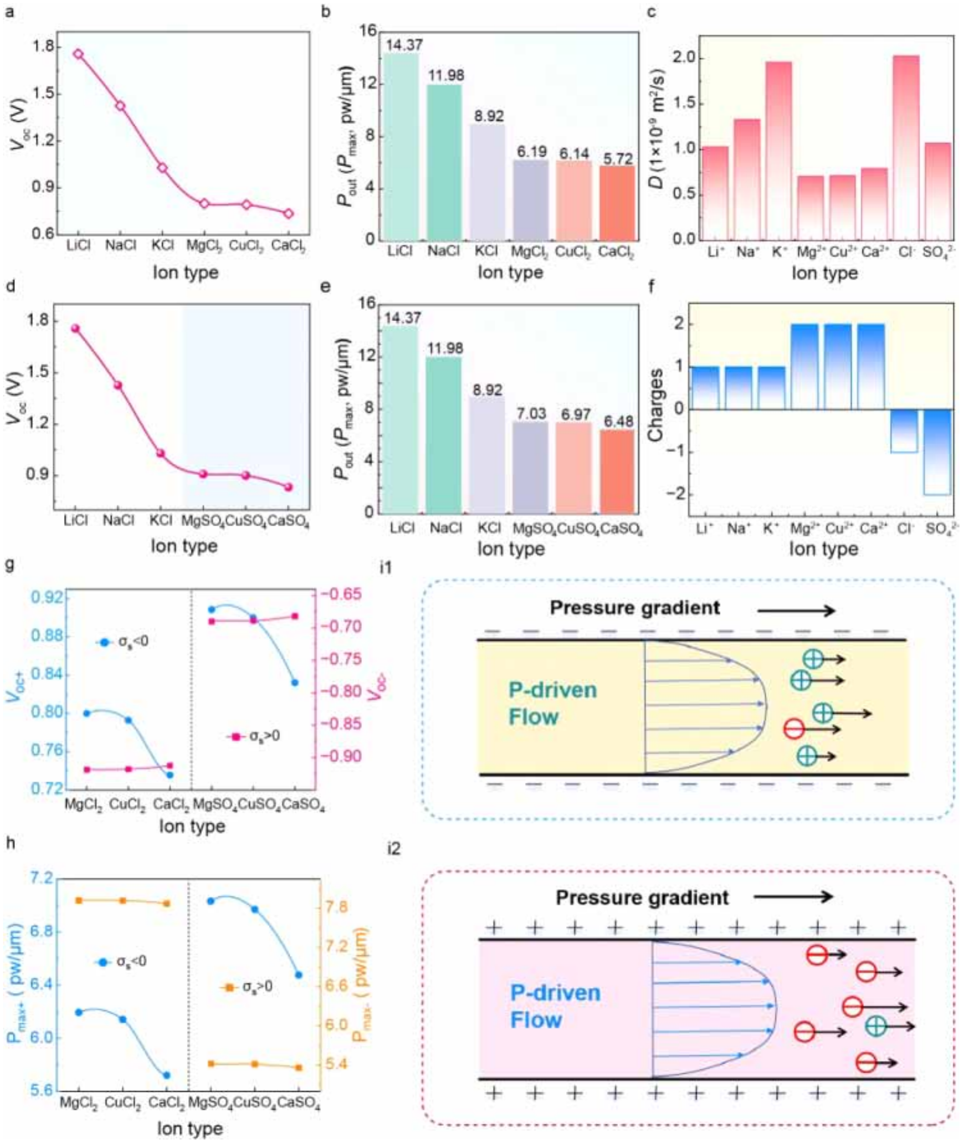

Figure 6. Effect of ion types on the output performance of the MF-NG. (a) Under the conditions of P = 5 bar, σ_s = −1 mC/m,^{2} and c_0 = 0.1 mM, the effect of cation valence and diffusion coefficient on the output voltage. (b) The effect of cation valence and diffusion coefficient on maximum output power. (c) Diffusion coefficients of different ions. (d) Effect of multivalent anion on the output voltage. (e) Effect of multivalent anion on the maximum power. (f) Charge number carried by the considered ions. (g) Effect of multivalent anion on the output voltage under positive and negative channel surface charge conditions. (h) Effect of multivalent anion on the maximum output power under positive and negative channel surface charge conditions. (i1) Schematic diagram of ion transport system under negative channel surface charge. (i2) Schematic diagram of ion transport system under positive channel surface charge.

judicious selection of the electrolyte solution is critical for optimizing MF-NG output performance.

3. CONCLUSIONS

In summary, we present a comprehensive theoretical model for a microfluidic nanogenerator (MF-NG) capable of converting fluidic hydropower into direct current (DC) power through the phenomenon of streaming potential. This unified model integrates the Poisson equation, Nernst−Planck equation, and Navier−Stokes equation to explore the electric double layer (EDL) electric field, ion transport processes, and the generation of streaming potentials as well as streaming-induced electric fields (Figure 7). A parametric study is conducted, varying applied pressure, surface charge density, solution concentration, and solute types, to examine the relationships between different excitation conditions and external electrical outputs. The physical mechanisms underlying the MF-NG and key properties of ion transport are fully quantified and visualized. Crucially, we elucidate the generation of displacement current within the microchannel and its relation to the net current. The key conclusions are as follows:

(1) When pressure is applied, co-ions accumulate at the channel inlet while counterions gather at the channel outlet. This phenomenon generates a reverse-flow streaming-induced electric field and a time-varying displacement current. In steady-state conditions, the strength of the streaming-induced electric field reaches its maximum, forming a streaming potential, at which point both the displacement current and net current approach zero.

(2) The displacement current remains balanced with the net current throughout the system, from equilibrium (no-

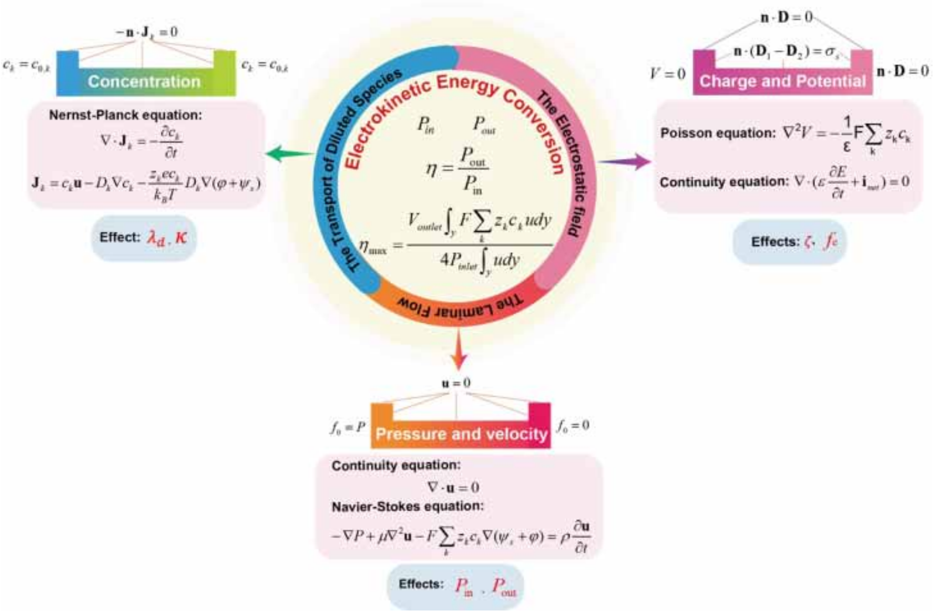

Figure 7. Schematic diagram of the numerical simulation approach for the MF-NG, including main governing equations, key parameters and their effects, boundary conditions, multiphysical field interaction coupling relationships, and energy conversion modes.

flow) to steady-state conditions. This displacement current serves as a measurable indicator of the evolving streaming-induced electric field, detailing the progress of mass transfer and charge transport within the microchannel.

(3) The thickness of the EDL, which determines the spatial utilization of the nonelectroneutral solution region, is inversely correlated with solution concentration. Lower solution concentrations lead to stronger streaming-induced electric fields along the flow direction and require more time for the pressure-driven system to reach steady state. However, as solution concentration increases, the total net charge transported decreases, while the peak displacement current rises with decreasing concentration. Notably, a low concentration can cause the electric double layers to overlap.

(4) An increase in surface charge density on the channel walls results in the accumulation of more counterions near the walls, altering the spatial distribution of the EDL. This change suppresses net ionic charge transfer and flow rate, ultimately impeding the development of the streaming potential. Additionally, less time is required for the displacement current to peak, and this peak value is positively correlated with surface charge density.

(5) Regarding the basic electrokinetic response properties of the MF-NG, numerical results indicate that the external outputs are extremely affected by the applied pressure, solution concentration, surface charge density, and ion species. We systematically elucidate the physical mechanisms and corresponding quantitative relationships among these macroscopic physical quantities.

3.1. Methods. The theoretical model for the microfluidic nanogenerator (MF-NG) is developed using COMSOL Multiphysics software, which integrates the Electrostatics (EC), Creeping Flow (CF), and Transport of Diluted Species (TDS) modules. The relevant equations, boundary conditions, and key physical effects are illustrated in Figure 7. The basic output performance and operational processes of the MF-NG are simulated by numerically solving these equations (Supplementary Notes 3 and 4). Detailed key equations for pressure-driven nanofluidic power generation, and equivalent circuit formulations for the MF-NG are present in Supplementary Notes 1 and 2, respectively. To calculate the electric double layer potential distribution and the space charge density, we utilize the Poisson equation:

$$\nabla^2 V = -\frac{1}{\varepsilon}F\sum_k z_k c_k \tag{2}$$

where V represents the electrical potential, ε is the dielectric constant, F is Faraday's constant, and z_k, c_k represent the valence and molar concentration of kth ion, respectively. The Creeping Flow module describes the pressure-driven flow field via the Navier−Stokes equations,

$$\rho\frac{\partial \boldsymbol{u}}{\partial t} = -\nabla P + \mu\nabla^2\boldsymbol{u} - \mathrm{F}\sum_k z_k c_k \nabla V \tag{3}$$

where ρ is the fluid density, t is time, P is the pressure, and μ is the coefficient of fluid viscosity.

The first term of eq 3 accounts for the inertial force of the fluid, while the right side consists of three components: the pressure gradient acting on the unit volume, viscous diffusion, and the force due to the electric field. Accompanying the Navier−Stokes equations is the continuity equation, which ensures conservation of mass for incompressible flow:

$$\nabla\cdot\boldsymbol{u} = 0 \tag{4}$$

The Transport of Diluted Species module models ion transport through the Nernst−Planck equation:

$$\nabla\cdot\boldsymbol{J}_k = -\frac{\partial c_k}{\partial t} \tag{5}$$

where $\boldsymbol{J}_k$ is,

$$\boldsymbol{J}_k = c_k\boldsymbol{u} - D_k\nabla c_k - \frac{e c_k z_k}{k_B T}D_k\nabla V \tag{6}$$

Note that J_k is the molar flux of the kth ion, signifying the quantity of ion substance traversing a unit area in a given direction per unit time. The convection term $c_k\boldsymbol{\mu}$ describes ion transport due to fluid flow, the diffusion term$-D_k\nabla c_k$ signifies ion movement from regions of high to low concentration, and the electromigration term $\frac{ec_kz_k}{k_BT}D_k\nabla V$ accounts for ion drift under the influence of the electric field, with D_k being the diffusion coefficient of the kth ion. In summary, the fluid dynamics within the channel are modeled within the framework of the Navier–Stokes equations, while the relevant charge distribution and ion transport phenomena are described by the Poisson–Nernst–Planck (PNP) formulation.

ASSOCIATED CONTENT

Supporting Information

The Supporting Information is available free of charge at https://pubs.acs.org/doi/10.1021/acsnano.5c15914.

> Key equations for pressure-driven nanofluidic power generation (Supplementary Note 1); equivalent circuit formulations for nanofluidic power generation (Supplementary Note 2); mesh discretization and modeling methodology (Supplementary Note 3); modeling details for the MF-NG (Supplementary Note 4); additional figures showing basic output characteristics of the microfluidic nanogenerators (PDF)

AUTHOR INFORMATION

Corresponding Authors

Jiajia Shao – *Beijing Institute of Nanoenergy and Nanosystems, Chinese Academy of Sciences, Beijing 101400, P. R. China; School of Nanoscience and Technology, University of Chinese Academy of Sciences, Beijing 100049, P. R. China;* orcid.org/0000-0002-9777-1930; Email: shaojiajia@binn.cas.cn

Zhong Lin Wang – *Beijing Institute of Nanoenergy and Nanosystems, Chinese Academy of Sciences, Beijing 101400, P. R. China; School of Nanoscience and Technology, University of Chinese Academy of Sciences, Beijing 100049, P. R. China;* Email: zlwang@gatech.edu

Shuge Dai – *School of Physics, Zhengzhou University, Zhengzhou 450052, P. R. China;* Email: shugedai@zzu.edu.cn

Authors

Jingwen Zhang – *School of Physics, Zhengzhou University, Zhengzhou 450052, P. R. China*

Hadrien Monluc – *Université Paris-Saclay, CentraleSupélec, ENS Paris-Saclay, CNRS, LMPS - Laboratoire de Mécanique Paris-Saclay, Gif-sur-Yvette 91190, France*

Di Wei – *Beijing Institute of Nanoenergy and Nanosystems, Chinese Academy of Sciences, Beijing 101400, P. R. China;* orcid.org/0000-0003-2670-6362

Jing You – *Australian Research Council Center of Excellence in Future Low Energy Electronics Technologies, University of Wollongong, Wollongong, New South Wales 2500, Australia*

Liyun Ma – *The Hamlyn Centre for Robotic Surgery, Department of Mechanical Engineering, Imperial College London, London SW7 9AG, United Kingdom;* orcid.org/0000-0002-5860-7636

Liming Ding – *School of Chemical Engineering and Light Industry, Guangdong University of Technology, Guangzhou 510006, P. R. China;* orcid.org/0000-0001-6437-9150

Complete contact information is available at: https://pubs.acs.org/10.1021/acsnano.5c15914

Author Contributions

Z.L.W. conceived and designed the project. J.J.S. and S.G.D. supervised the work. J.W.Z. and H.M. performed the theoretical model. J.W.Z. and J.J.S. contributed to the theoretical calculations . Z.L.W., J.J.S., S.G.D., J.W.Z., H.M., D.W., J.Y., L.M.D., and L.Y.M. took part in the discussion and gave important suggestions. All authors approved the final version of the manuscript.

Notes

The authors declare no competing financial interest.

ACKNOWLEDGMENTS

This work was supported by the Beijing Natural Science Foundation (2252062, 24ISB012, IS23037); the Youth Innovation Promotion Association, Chinese Academy of Sciences; the National Key R&D Project from the Ministry of Science and Technology (2023YFB3208100); and the National Key Research and Development Program of China (2022YFB3803300, 2023YFE0116800).

REFERENCES

(1) Van der Heyden, F.; Stein, D.; Dekker, C. Streaming currents in a single nanofluidic channel. *Phys. Rev. Lett.* **2005**, *95* (11), 116104.

(2) Newaz, A.; Markov, D.; Prasai, D.; Bolotin, K. Graphene transistor as a probe for streaming potential. *Nano Lett.* **2012**, *12* (6), 2931–2935.

(3) Wang, Y.; Gao, S.; Xu, W.; Wang, Z. Nanogenerators with superwetting surfaces for harvesting water/liquid energy. *Adv. Funct. Mater.* **2020**, *30* (26), 1908252.

(4) Zhang, R.; Wang, S.; Yeh, M.; Pan, C.; Lin, L.; Yu, R.; Zhang, Y.; Zheng, L.; Jiao, Z.; Wang, Z. A streaming potential/current-based microfluidic direct current generator for self-powered nanosystems. *Adv. Mater.* **2015**, *27* (41), 6482–6487.

(5) Liu, K.; Ding, T.; Mo, X.; Chen, Q.; Yang, P.; Li, J.; Xie, W.; Zhou, Y.; Zhou, J. Flexiblemicrofluidic nanogenerator based on electrokinetic conversion. *Nano Energy* **2016**, *30*, 684–690.

(6) Lu, M.-C.; Satyanarayana, S.; Karnik, R.; Majumdar, A.; Wang, C.-C. A mechanical-electrokinetic battery using a nano-porous membrane. *J. Micromech. Microeng.* **2006**, *16* (4), 667.

(7) Zhou, T.; He, X. H.; Zhao, J.; Shi, L.; Wen, L. P. Electrokinetic transport of nanoparticles in functional group modified nanopores. *Chin. Chem. Lett.* **2023**, *34*, 107667.

(8) Mansouri, A.; Bhattacharjee, S.; Kostiuk, L. Electrokinetic energy conversion by microchannel array: electrical analogy, experiments, and electrode polarization. *J. Phys. Chem. C* **2014**, *118* (42), 24310–24324.

(9) Schmickler, W. Electronic effects in the electric double layer. *Chem. Rev.* **1996**, *96* (8), 3177–3200.

(10) Hunter, R. J.*Zeta potential in colloid science: Principles and applications*Academic Press2013

(11) Lyklema, J. *Fundamentals of Interface and Colloid Science, 2: Solid-Liquid Interfaces*; Academic Press, 1995.

(12) Donath, E.; Voigt, A. Streaming current and streaming potential on structured surfaces. *J. Colloid Interface Sci.* **1986**, *109* (1), 122–139.

(13) Szymczyk, A.; Zhu, H.; Balannec, B. Pressure-driven ionic transport through nanochannels with inhomogeneous charge distributions. *Langmuir* **2010**, *26* (2), 1214–1220.

(14) Lee, K.; Zhang, Y. Z.; Jiang, Q.; Kim, H.; Alkenawi, A. A.; Alshareef, H. N. Ultrasound-driven two-dimensional $Ti_3C_2T_x$ MXene hydrogel generator. *ACS Nano* **2020**, *14* (3), 3199–3207.

(15) Yang, G.; Lei, W.; Chen, C.; Qin, H.; Zhang, L.; Su, Y.; Wang, J.; Chen, Z.; Sun, L.; Wang, X.; Liu, D. Ultrathin $Ti_3C_2T_x$ (MXene)

membrane for pressure-driven electrokinetic power generation. *Nano Energy* **2020**, *75* (10), 104954.

(16) Yin, J.; Zhou, J.; Fang, S.; Guo, W. Hydrovoltaic energy on the way. *Joule* **2020**, *4* (9), 1852−1855.

(17) Wang, Z. On Maxwell's displacement current for energy and sensors: the origin of nanogenerators. *Mater. Today* **2017**, *20* (2), 74−82.

(18) Wang, Z. L.; Shao, J. Recent progress on the maxwell's equations for describing a mechano-driven medium system with multiple moving objects/media. *Electromagn. Sci.* **2023**, *1* (2), 0020171.

(19) Lin, S.; Chen, X.; Wang, Z. Contact electrification at the liquid-solid interface. *Chem. Rev.* **2022**, *122* (5), 5209−5232.

(20) Wang, Z.; Wang, A. On the origin of contact-electrification. *Mater. Today* **2019**, *30* (5), 34−51.

(21) Brown, M.; Goel, A.; Abbas, Z. Effect of electrolyte concentration on the Stern layer thickness at a charged interface. Angew. *Chem. Int. Ed.* **2016**, *128* (11), 3854−3858.

(22) Clogston, J.; Patri, A. Zeta potential measurement. *Methods Mol. Biol.* **2011**, *697* (19), 63−70.

(23) Stern, E.; Wagner, R.; Sigworth, F.; Breaker, R.; Fahmy, T.; Reed, M. Importance of the Debye screening length on nanowire field effect transistor sensors. *Nano Lett.* **2007**, *7* (11), 3405−3409.

(24) He, X. H.; Xin, W. W.; Yang, C. W.; Wan, S.; Liu, T.; Huang, S.; Deng, Y.; Shi, L.; Wen, L. P.; Zhou, T. Two-dimensional molybdenum disulfide/graphene oxide composite membrane for stable osmotic energy conversion. *J. Membr. Sci.* **2025**, *732*, 124251.

(25) Daiguji, H.; Yang, P.; Szeri, A.; Majumdar, A. Electrochemomechanical energy conversion in nanofluidic channels. *Nano Lett.* **2004**, *4* (12), 2315−2321.

(26) Peng, R.; Li, T.; Song, H.; Wang, S.; Song, Y.; Wang, J.; Xu, M. In-depth understanding of boosting salinity gradient power generation by ionic diode. *iScience* **2023**, *26* (7), 107184.

(27) Zhou, T.; Liu, T.; Huang, S.; He, X. H.; Zhao, J.; Shi, L. Y.; Yan, H.; Wen, L. P. The influence of divalent ions on the osmotic energy conversion performance of 2D cation exchange membrane in reverse electrodialysis process. *Desalination* **2024**, *591*, 118036.